

# Resonant high frequency topological Hall conductivity from skyrmions

Sopheak Sorn,<sup>1,\*</sup> Luyi Yang,<sup>2</sup> and Arun Paramakanti<sup>1,†</sup>

<sup>1</sup>*Department of Physics, University of Toronto, Toronto, Ontario M5S1A7, Canada.*

<sup>2</sup>*State Key Laboratory of Low Dimensional Quantum Physics,  
Department of Physics, Tsinghua University, Beijing 100084, China*

(Dated: May 27, 2022)

We study the high frequency Hall conductivity in a two-dimensional (2D) model of conduction electrons coupled to a background magnetic skyrmion texture via an effective Hund's coupling term. For an ordered skyrmion crystal, a Kubo formula calculation using the basis of skyrmion crystal Chern bands reveals a resonant Hall response at a frequency set by the Hund's coupling:  $\hbar\omega_{\text{res}} \approx J_H$ . A complementary real-space Kubo formula calculation for an isolated skyrmion in a box reveals a similar resonant Hall response. A linear relation between the area under the Hall resonant curve and the skyrmion density is discovered numerically and is further elucidated using a gradient expansion which is valid for smooth textures and a local approximation based on a spin-trimer calculation. We point out the issue of distinguishing this skyrmion contribution from a similar feature arising from spin-orbit interactions, as demonstrated in a model for Rashba spin-orbit coupled electrons in a collinear ferromagnet, which is analogous to the difficulty of unambiguously separating the d.c. topological Hall effect from the anomalous Hall effect. The resonant feature in the high frequency topological Hall effect is proposed to provide a potentially useful local optical signature of skyrmions via probes such as scanning magneto-optical Kerr microscopy.

## I. INTRODUCTION

Originally proposed in particle physics [1], skyrmions are realized in many condensed matter systems as non-coplanar magnetic swirls with a non-trivial integer topological invariant. The topological nature of skyrmions provides them with a sense of robustness against small perturbations, which, together with their small sizes, have made them promising candidates for realizing future dense data-storage technology [2–5]. The stabilization, manipulation, and detection of skyrmions have thus emerged as a central theme which has attracted immense research interest in the fundamental and applied aspects of skyrmion physics [5]. Skyrmions have been found in both isolated and crystalline forms in a wide range of magnetic solids [6] including quantum Hall systems [7, 8], non-centrosymmetric magnetic systems [9–16], and frustrated magnets [17–20]. Recently, skyrmions have even been proposed in two-channel Kondo lattice systems where two channels of conduction electron are Kondo coupled symmetrically to a lattice of Kondo spins [21]. At low temperature, the channel  $SU(2)$  symmetry is spontaneously broken by the Kondo effect, leading to a “ferromagnetic” ordering of a spinor-like order parameter. Skyrmions then appear as topological defects in the “ferromagnetic” phase [21], and they have been shown to support movable Majorana zero modes, providing a new, potential platform for realizing topological quantum computation [22]. Skyrmions have also been proposed to drive superconductivity in twisted bilayer graphene [23].

In experiments, magnetic skyrmions can be detected directly by visualizing the real-space profile of their out-

of-plane and in-plane spin components using magnetic force microscopy [16, 24, 25] and Lorentz transmission electron microscopy [13, 20, 26] respectively. Other techniques suitable for detecting and studying crystals of skyrmions include X-ray [18–20] and neutron diffraction [11, 12]. In metallic magnets, the noncoplanarity of the skyrmion spin texture imprints a real-space Berry phase on the conduction electrons [27, 28]. The extra Berry phase can be regarded as an emergent magnetic field seen by the electrons, thereby inducing an additional Hall effect known as the topological Hall effect (THE), first observed in MnSi [9, 10], which provides an indirect transport probe of skyrmions. In addition to charge transport, the real-space Berry phase also affects heat flow through topological Nernst [29, 30] and thermal Hall effects [31]. However, there is growing evidence of examples in thin films where the ostensible appearance of THE may in fact be an additional Hall effect contribution stemming from inhomogeneous magnetic domains and domain wall scattering [32–38]. Hence, one generally needs complementary imaging probes to confirm the existence of skyrmions.

While the impact of skyrmions on electronic charge and heat transport properties has been actively studied, their impact on electronic optical properties remains less explored. To fill in this gap, we examine in this paper the nonzero-frequency Hall conductivity in a model of conduction electrons coupled to skyrmions via an effective Hund's coupling  $J_H$ .

The band structure of electrons coupled to local moments is conveniently divided into two sectors containing electronic states whose spins are locally parallel or anti-parallel to the underlying skyrmion spins. For a skyrmion crystal (SkX), each sector supports bands with nontrivial Chern numbers as a result of the real-space Berry phase; this Berry phase can be regarded as a fic-

\* [ssorn@physics.utoronto.ca](mailto:ssorn@physics.utoronto.ca)

† [arunp@physics.utoronto.ca](mailto:arunp@physics.utoronto.ca)

titious Aharonov-Bohm flux which leads to an effective electronic Hofstadter model. We use the Kubo formula to compute the resulting a.c. Hall conductivity, uncovering nontrivial frequency dependence in two frequency windows. The structure at low frequency is set by the energy gap between neighboring Chern bands, while the high frequency response near  $\hbar\omega \approx J_H$  exhibits a resonance originating from a large number of intersector spin-flip transition channels between pairs of Chern bands which disperse similarly and differ in energy by a similar amount of  $J_H$ . We show that the high frequency resonance is robust, occurring also for isolated skyrmions, as demonstrated by a real-space Kubo formula computation for a skyrmion in a box. We provide an analytical understanding of this resonance through a smooth texture approximation and a local spin-trimer calculation. These show that the area under resonance of  $\text{Im} \sigma_{xy}$  scales linearly with the skyrmion density  $\rho_{sk}$ .

The nontrivial high-frequency topological Hall effect is expected to be manifest in experiments such as scanning Kerr microscopy, magneto-optical Kerr effect, and Faraday effect. Materials hosting a large density of skyrmions, such as  $\text{Gd}_2\text{PdSi}_3$  [18],  $\text{Gd}_3\text{Ru}_4\text{Al}_{12}$  [19],  $\text{GdRu}_2\text{Si}_2$  [20], and  $\text{MnGe}$  [12], are likely to be viable candidates for observing the non-zero-frequency topological Hall effect and its resonant feature.

The paper is organized as the following. Section II introduces a triangular-lattice model of conduction electrons coupled to a spin texture, and the spin textures studied in this work. Section III is devoted to properties of the SkX spin texture, encompassing its electronic band structures, conductivity spectra featuring the Hall resonance, and the numerical linear scaling of the area under the resonance with the skyrmion density. In Section IV, this scaling relation is explained by an analytical expression obtained from a smooth texture approximation. In Section V, we present the study of a “skyrmion in a box” and show that the resonance is robust and occurs even when the spin texture contains only a single skyrmion. Section VI discusses an analytical understanding of how this resonance occurs even in the minimal setting with three sites, i.e. a spin trimer, hosting a noncoplanar spin configuration. Based on this analytical spin trimer result, we try to understand the Hall resonance in the SkX case and the skyrmion-in-a-box case as a local spatial average over triangular plaquettes. In Section VII, we discuss how spin orbit coupling in a uniform ferromagnet can also produce a resonance feature similar to skyrmions, and how it may complicate the issue of extracting the skyrmion contribution to the resonant optical Hall response. We conclude in Section VIII with a discussion of how the spatial variation of the imaginary part of the Hall conductivity at the resonant frequency, using tools such as scanning Kerr microscopy, might serve as a useful optical probe of skyrmions and SkX.

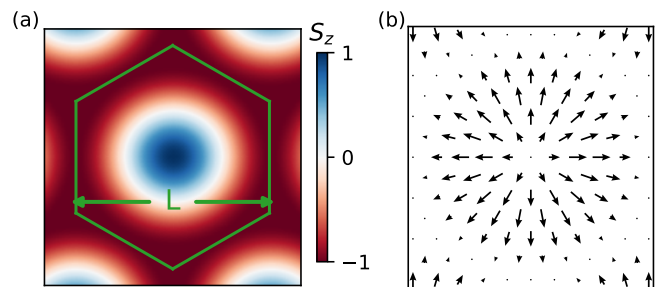


FIG. 1. Triangular SkX spin texture. (a) Color plot illustrating the profile of the  $z$ -component of the spin texture with a hexagonal unit cell whose width is given by  $L$ . Each unit cell contains a Néel skyrmion with a radius  $R = L/2$ . (b) Profile of the in-plane spin components.

## II. MODEL

We consider a triangular-lattice model of electrons hopping on nearest-neighbor bonds, sensing a spin-dependent potential of a background spin texture  $\{\mathbf{S}_i\}$  via an effective ferromagnetic Hund’s coupling  $J_H > 0$ . The Hamiltonian is given by [39–41]

$$H_0 = -t \sum_{\langle ij \rangle} \left( c_{i\sigma}^\dagger c_{j\sigma} + c_{j\sigma}^\dagger c_{i\sigma} \right) - J_H \sum_i \hat{\mathbf{s}}_i \cdot \mathbf{S}_i, \quad (1)$$

where  $\hat{\mathbf{s}}_i = \frac{1}{2} c_{i\sigma}^\dagger \boldsymbol{\sigma}_{\sigma\sigma'} c_{i\sigma'}$  is the electron spin operator,  $\boldsymbol{\sigma} = (\sigma_x, \sigma_y, \sigma_z)$  are the Pauli matrices, and  $\mathbf{S}_i$  is a unit-norm classical spin vector at site  $i$  of the spin texture. We set the lattice constant of the triangular lattice  $a = 1$ .

We consider two configurations to numerically solve for the electronic properties: (i) a triangular crystal of Néel skyrmions commensurate with the underlying triangular lattice, and (ii) an open-boundary hexagonal box containing one skyrmion.

Figure 1 illustrates the SkX spin texture with a hexagonal unit cell of width  $L$  containing one Néel skyrmion and enclosing  $L^2$  sites. The hexagonal box is obtained by simply cutting out a single unit cell from the lattice. Within the hexagonal box (unit cell), the skyrmion texture is defined by a circular ansatz [42]

$$\mathbf{S}_i = (\sin \theta(\mathbf{r}_i) \cos \phi(\mathbf{r}_i), \sin \theta(\mathbf{r}_i) \sin \phi(\mathbf{r}_i), \cos \theta(\mathbf{r}_i)), \quad (2)$$

where  $\mathbf{r}_i = \mathbf{r}_i - \mathbf{r}_\square$  is the position of the  $i$ -th site relative to the center  $\mathbf{r}_\square$  of the hexagonal box (unit cell).

$$\theta(\mathbf{r}_i) = \begin{cases} \frac{\pi |\mathbf{r}_i|}{R} & \text{for } |\mathbf{r}_i| < R, \\ 0 & \text{otherwise,} \end{cases}, \quad (3)$$

$$\cos \phi(\mathbf{r}_i) = \frac{\mathbf{r}_{i,x}}{|\mathbf{r}_i|}; \quad \sin \phi(\mathbf{r}_i) = \frac{\mathbf{r}_{i,y}}{|\mathbf{r}_i|}, \quad (4)$$

where  $\mathbf{r}_{i,x(y)}$  is the  $x(y)$ -component of  $\mathbf{r}_i$ .

In the remainder of the paper, we fix the skyrmion radius  $R = L/2$ , with  $R \gg 1$  for large skyrmions. We will quote the value of  $R$  when discussing variation of the optical response with skyrmion size.

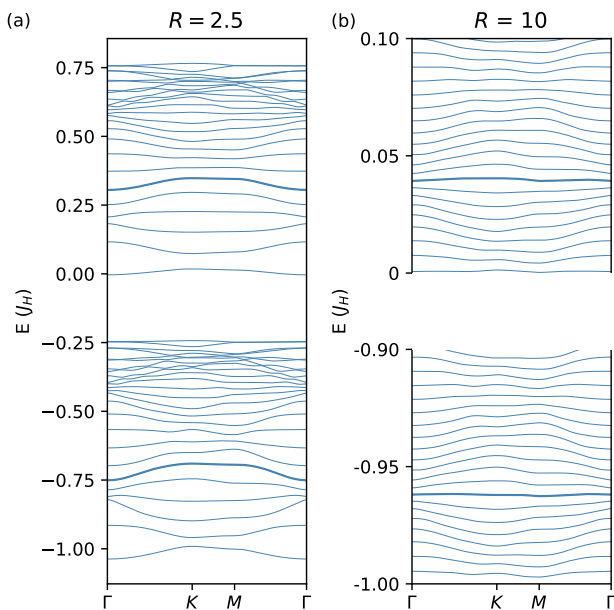


FIG. 2. Band structures corresponding to the SkX with (a)  $R=2.5$  and (b)  $R=10$ , with  $J_H=10t$ . The band structures consist of Chern bands grouped into a low energy parallel sector and a high energy anti-parallel sector. Bold bands illustrate an example of pairs of similarly dispersing low and high energy Chern bands differing in energy by an amount  $\sim J_H$ , which leads to a resonant feature in the a.c. conductivity at  $\hbar\omega \approx J_H$  as shown later.

### III. SKYRMION CRYSTAL

In this section, we focus on the properties of a SkX, including its electronic bands, high frequency resonance in the Hall response, and the scaling of the resonant feature with the skyrmion density.

#### A. Electronic bands

Figure 2 shows the band structures corresponding to the SkX with  $R=2.5$  in panel (a) and  $R=10$  in panel (b) when  $J_H=10t$ . These bands are shown along high-symmetry lines of the mini-Brillouin zone (BZ) obtained from folding the original BZ of the underlying triangular lattice. Given the large  $J_H/t \gg 1$ , the bands group into a low-energy sector and a high-energy sector, differing in energy by  $J_H$ , corresponding to states where the electron spins are locally parallel and anti-parallel, respectively, to the underlying skyrmion spins. To highlight this, the energy in Figure 2 is measured in units of  $J_H$ . Each sector has  $L^2 = 4R^2$  bands, with a bandwidth  $W \approx 9t$ , so the average energy spacing between a pair of neighboring bands is  $W/4R^2$ ; for our choice of  $J_H/t=10$  this corresponds to a level separation  $\sim J_H/4R^2$ .

These bands have non-trivial Chern numbers due to the real-space Berry phase picked up by electrons as they

traverse the skyrmion texture, which admits an effective description of the two sectors using generalized Hofstadter models carrying opposite fluxes [40, 43–46]. We find pairs of similarly dispersing Chern bands, one from the parallel sector and the other from the anti-parallel sector, as illustrated by the bold bands in Fig.2. They differ in energy by a similar amount of roughly  $J_H$ , resulting in a number of optical transition channels at this energy, which will be shown later to cause a resonance feature in the a.c. conductivity at  $\hbar\omega_{\text{res}} \approx J_H$ .

The following linear response Kubo formula is used to study the a.c. conductivity tensor  $\sigma_{\alpha\beta}(\omega)$  [47, 48]:

$$\sigma_{\alpha\beta} = \frac{i\hbar e^2}{\mathcal{A}} \sum_{\mathbf{k}mn} \frac{f(E_{\mathbf{k}n}) - f(E_{\mathbf{k}m})}{E_{\mathbf{k}m} - E_{\mathbf{k}n}} \frac{(v_{\mathbf{k}\alpha})_{nm} (v_{\mathbf{k}\beta})_{mn}}{\hbar\omega + i\gamma + E_{\mathbf{k}n} - E_{\mathbf{k}m}}, \quad (5)$$

where  $\alpha, \beta = x, y$ , and  $\hbar(v_{\mathbf{k}\alpha})_{nm} \equiv \langle \mathbf{k}n | \frac{\partial \mathcal{H}(\mathbf{k})}{\partial k_\alpha} | \mathbf{k}m \rangle$  is a matrix element of the velocity operator between the Bloch states  $|\mathbf{k}n\rangle$  and  $|\mathbf{k}m\rangle$  corresponding to the energy eigenvalues  $E_{\mathbf{k}n}$  and  $E_{\mathbf{k}m}$  respectively.  $\mathcal{H}(\mathbf{k})$  is the Hamiltonian matrix,  $f$  is the Fermi distribution,  $\mathcal{A}$  is the area of the 2D system, and  $\gamma$  is a small broadening. To study the open-boundary skyrmion in a box, the Kubo formula is modified into a real-space version where the composite label  $(\mathbf{k}, m)$  is replaced with the energy level label. Similar to the SkX case, the current operator  $\mathbf{j} = -e\mathbf{v}$  can be obtained from  $\delta H_0[\mathbf{A}]/\delta \mathbf{A}$  (see e.g. Appendix A of Ref.[38] for more details), where  $\mathbf{A}$  is the vector potential of the externally applied field, and  $H_0[\mathbf{A}]$  is the Hamiltonian after the Peierls substitution. In the rest of the paper, we fix parameters  $\gamma = 0.05t$ ,  $J_H = 10t$ , and set the electron filling to  $1/6$ .

#### B. Frequency dependent conductivity in a skyrmion crystal

Figure 3 shows  $\sigma_{xy}(\omega)$  and  $\sigma_{xx}(\omega)$  obtained from the Kubo formula for the SkX with  $R=2.5$ , which corresponds to the band structure in Fig.2(a).  $\sigma_{xy}$  and  $\sigma_{xx}$  exhibit nontrivial frequency dependence in two windows, one at small frequency set by the average energy gap between neighboring Chern bands, and the other occurring around  $J_H$ . The former arises from intra-sector transitions among Chern bands within the parallel sector, while the latter originates from inter-band spin-flip transitions between Chern bands in the parallel sector and those in the anti-parallel sector. The dissipative parts of the conductivity tensor,  $\text{Re } \sigma_{xx}$  and  $\text{Im } \sigma_{xy}$ , can be shown to track the joint density of state (JDOS) of the optical transitions  $\propto \sum_{\mathbf{k}} \sum_{E_{\mathbf{k}n} < \mu} \sum_{E_{\mathbf{k}m} > \mu} \delta(\hbar\omega - E_{\mathbf{k}m} + E_{\mathbf{k}n})$ , where  $\mu$  is the chemical potential. The non-dissipative parts,  $\text{Im } \sigma_{xx}$  and  $\text{Re } \sigma_{xy}$  correspondingly exhibit a frequency dependence consistent with Kramers-Krönig relations given the above dissipative response. In the high-frequency window, the JDOS peaks at  $\hbar\omega \approx J_H$  as a result of having a number of transition channels due to the presence of many similarly dispersing pairs of Chern

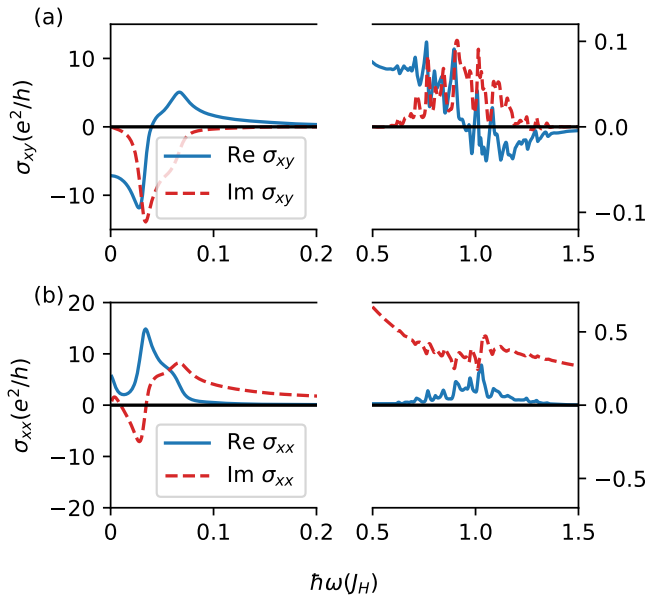


FIG. 3. Spectrum of (a)  $\sigma_{xy}$  and (b)  $\sigma_{xx}$  for a small SkX unit cell  $L=5$  with a skyrmion radius  $R=2.5$  which corresponds to the band structure in Fig.2(a). Two windows of nontrivial frequency dependence are seen: (1) a low frequency regime set by the average energy gap between neighboring Chern bands and (2) a high frequency regime around  $\hbar\omega \approx J_H$ . The former originates from transitions among Chern bands within the same, parallel-spin sector, whereas the later arises from spin-flip transitions across pairs of Chern bands which disperse similarly and differ in energy by  $\approx J_H$ .

bands differing in energy by a similar amount of roughly  $J_H$ , as mentioned in the previous section. For a SkX with a small  $R$ , the average energy gap  $W/4R^2$  is significant, so that the Chern bands are well-separated, and the conductivity spectrum displays discrete peaks.

Upon increasing the skyrmion size and the corresponding periodicity of the SkX, the small-frequency window shifts towards zero as the energy gap between neighboring Chern bands shrinks. However, the high-frequency transition remains at around  $J_H$ , being set by the local spin-flip energy gap. This is illustrated in Fig.4 which shows  $\sigma_{xy}(\omega)$  and  $\sigma_{xx}(\omega)$  for a SkX with  $R=10$  whose band structure is given by Fig.2(b). Due to the shrunken energy gap between adjacent levels, the discrete peaks seen earlier have merged with one another to form a Lorentzian-like resonant curve of JDOS peaking around  $J_H$ , which can again be traced back to the presence of many similarly dispersing pairs of Chern bands.

### C. Scaling of resonance with skyrmion density

We next examine the scaling of the Hall resonance with the areal skyrmion density  $\rho_{sk} = 2/\sqrt{3}L^2$  by varying  $L = 2R$ . Figure 5(a) shows the Kubo results for  $\text{Im } \sigma_{xy}$  near  $J_H$ , for  $L = 20, \dots, 25$ . As shown in Fig.5(b), the

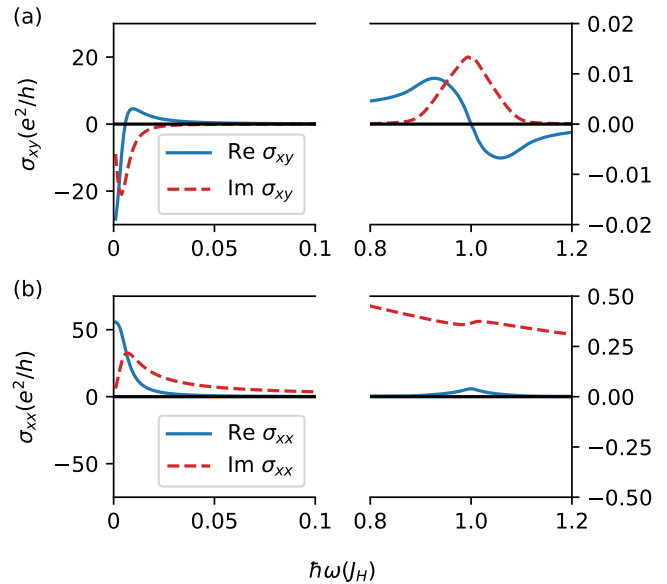


FIG. 4. Spectrum of (a)  $\sigma_{xy}$  and (b)  $\sigma_{xx}$  for a larger SkX unit cell  $L=20$  and larger-radius skyrmion  $R=10$ , corresponding to the band structure in Fig.2(b). While the low energy response moves to lower frequency due to the smaller energy separation between neighboring Chern bands, the large-energy response remains around  $\hbar\omega \approx J_H$ . Due to the smaller separation between neighboring Chern bands, the response shows a smooth Lorentzian behavior. The resonant peaks in  $\text{Im } \sigma_{xy}$  and  $\text{Re } \sigma_{xx}$  near  $J_H$  originate from spin-flip transitions involving many pairs of ‘energy-nested’ Chern bands.

areas under the resonant curves in panel (a) vary linearly with  $\rho_{sk}$ . In the next section, we derive this result using a smooth-texture approximation on the Kubo formula.

## IV. SMOOTH-TEXTURE APPROXIMATION FOR THE HALL RESONANCE

In this section, we elucidate the Lorentzian-like shape of the Hall resonance and the linear relation between  $\rho_{sk}$  and the area under resonance of  $\text{Im } \sigma_{xy}$  which can be estimated by applying a smooth texture approximation on the Kubo formula. Our main result in this section is that the area under the resonant imaginary Hall conductivity is given by

$$S \equiv \int d\omega \text{Im} \sigma_{xy}^{\text{res}}(\omega) \approx \frac{e^2 \pi t^2}{\hbar^2} \frac{N_{sk}}{J_H} \frac{\mathcal{F}}{\mathcal{A}} \quad (6)$$

where the numerical factor  $\mathcal{F}$  involves a momentum integral which depends on the electron filling; we give its explicit form in Appendix A. This result reproduces the linear scaling with skyrmion density  $N_{sk}/\mathcal{A}$  which we have observed numerically in the previous section; we will see later that a similar numerical scaling is also obtained for a single ‘skyrmion in a box’ problem.

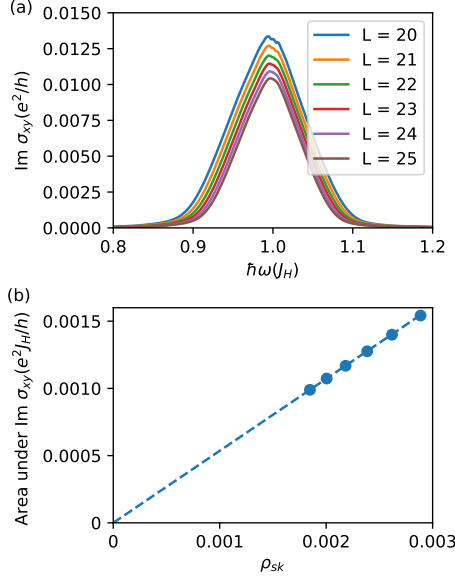


FIG. 5. (a) Resonant feature in  $\text{Im } \sigma_{xy}$  near  $J_H$  from numerical Kubo calculation for SkXs with varying unit cell size  $L$ . (b) Linear relation between  $\rho_{sk}$  and area under  $\text{Im } \sigma_{xy}$  resonance obtained from the curves shown in panel (a).

With somewhat less rigor, we can show that the Hall conductivity near the resonance behaves as

$$\sigma_{xy}^{\text{res}}(\omega) \approx -\frac{e^2 N_{sk}}{\hbar} \frac{t^2}{\mathcal{A}} \frac{\mathcal{F}}{J_H \hbar\omega - J_H + i\tilde{\gamma}} \quad (7)$$

where  $\tilde{\gamma} \propto t$  is an effective broadening (which decreases roughly as  $1/R$  with increasing skyrmion size).

The above results are obtained in two steps. We begin by expressing the Kubo formula in a local basis, where the spin quantization axis at each site is taken to be the direction of the skyrmion spin. In a second step, we

replace certain matrix elements by their simplified values for a corresponding uniform ferromagnet. This second step becomes increasingly accurate in the limit where the SkX spin texture varies slowly in space, namely large  $L$ , when the neighboring spins are almost parallel. The local basis we use is defined via eigenfunctions of the Hund's coupling term, so that

$$\begin{pmatrix} c_{i\uparrow} \\ c_{i\downarrow} \end{pmatrix} = \mathbf{m}_i \cdot \boldsymbol{\sigma} \begin{pmatrix} p_i \\ a_i \end{pmatrix}, \quad (8)$$

$$\mathbf{m}_i = \begin{pmatrix} \sin \frac{\theta_i}{2} \cos \phi_i, \sin \frac{\theta_i}{2} \sin \phi_i, \cos \frac{\theta_i}{2} \end{pmatrix}^T, \quad (9)$$

where  $p_i$  and  $a_i$  denote the electron annihilation operators for electron at site  $i$  whose spin is parallel and antiparallel to  $\mathbf{S}_i$  respectively, while  $\theta_i$  and  $\phi_i$  are defined in Section II. In this basis, the Hamiltonian is

$$H_0 = -J_H \sum_i (p_i^\dagger p_i - a_i^\dagger a_i) + H_{pp} + H_{aa} + H_{ap} + H_{pa} \quad (10)$$

$$H_{pp} = \sum_{\langle ij \rangle} (T_{pp,ij} p_i^\dagger p_j + h.c.), \quad (11)$$

$$H_{aa} = \sum_{\langle ij \rangle} (T_{aa,ij} a_i^\dagger a_j + h.c.), \quad (12)$$

$$H_{pa} = H_{ap}^\dagger = \sum_{\langle ij \rangle} (T_{pa,ij} p_i^\dagger a_j + T_{pa,ji} p_j^\dagger a_i) \quad (13)$$

The local unitary rotation leads to the spin texture being absorbed into effective complex hopping amplitudes  $T_{ij}$ .  $H_{pp}$  and  $H_{aa}$  then appear as generalized Hofstadter models of spinless fermions,  $p^\dagger$  and  $a^\dagger$ , which see opposite Berry fluxes as determined by these hopping integrals [40]. These fluxes can be viewed as an emergent magnetic field, which is responsible for the topological Hall effect. The hopping integrals are given by

$$\begin{aligned} T_{ij} &= \begin{pmatrix} T_{pp,ij} & T_{pa,ij} \\ T_{ap,ij} & T_{aa,ij} \end{pmatrix} \\ &= -t \begin{pmatrix} \cos\left(\frac{\theta_i}{2}\right) \cos\left(\frac{\theta_j}{2}\right) + e^{-i(\phi_i - \phi_j)} \sin\left(\frac{\theta_i}{2}\right) \sin\left(\frac{\theta_j}{2}\right) & e^{-i\phi_j} \cos\left(\frac{\theta_i}{2}\right) \sin\left(\frac{\theta_j}{2}\right) - e^{-i\phi_i} \cos\left(\frac{\theta_j}{2}\right) \sin\left(\frac{\theta_i}{2}\right) \\ e^{i\phi_i} \cos\left(\frac{\theta_i}{2}\right) \sin\left(\frac{\theta_j}{2}\right) - e^{i\phi_j} \cos\left(\frac{\theta_i}{2}\right) \sin\left(\frac{\theta_j}{2}\right) & \cos\left(\frac{\theta_i}{2}\right) \cos\left(\frac{\theta_j}{2}\right) + e^{i(\phi_i - \phi_j)} \sin\left(\frac{\theta_i}{2}\right) \sin\left(\frac{\theta_j}{2}\right) \end{pmatrix} \quad (14) \end{aligned}$$

The following form of the Kubo formula for the Hall conductivity is useful for the discussion in this section [49].

$$\sigma_{xy}(\omega) = \frac{i}{\mathcal{A}\omega} \sum_{\mathbf{k}} \sum_{E_{\mathbf{k}n} < \mu} \sum_{E_{\mathbf{k}m} > \mu} \left[ \frac{\langle \mathbf{k}n | j_x | \mathbf{k}m \rangle \langle \mathbf{k}m | j_y | \mathbf{k}n \rangle}{\hbar\omega + i\gamma + E_{\mathbf{k}n} - E_{\mathbf{k}m}} - \frac{\langle \mathbf{k}n | j_y | \mathbf{k}m \rangle \langle \mathbf{k}m | j_x | \mathbf{k}n \rangle}{\hbar\omega + i\gamma - E_{\mathbf{k}n} + E_{\mathbf{k}m}} \right], \quad (15)$$

where  $\mathbf{j}$  is the current operator. For large  $\omega > 0$  relevant to the resonance, we can drop the second term in the square bracket. In the local basis, the current operator is  $\mathbf{j} = \mathbf{j}_{pp} + \mathbf{j}_{aa} + \mathbf{j}_{ap} + \mathbf{j}_{pa}$ . Near resonance, the optical transitions between the parallel and anti-parallel sectors are dominant, so that  $\mathbf{j}_{pp} + \mathbf{j}_{aa}$  can be neglected. The Kubo formula may thus be approximated by

$$\sigma_{xy}^{\text{res}}(\omega) \approx \frac{i\hbar}{\mathcal{A}J_H} \sum_{\mathbf{k}, m, n} \left[ \frac{\langle P\mathbf{k}n | j_{pa}^x | A\mathbf{k}m \rangle \langle A\mathbf{k}m | j_{ap}^y | P\mathbf{k}n \rangle}{\hbar\omega + i\gamma + E_{\mathbf{k}n}^P - E_{\mathbf{k}m}^A} \right], \quad (16)$$

where we have replaced the frequency in the prefactor by its value  $J_H$  on resonance, and the prime on the sum indicates a restriction to  $E_{\mathbf{k}n} < \mu$  and  $E_{\mathbf{k}m} > \mu$ . The current operators are explicitly given by

$$\mathbf{j}_{pa} = -\frac{ie}{\hbar} \sum_{\langle ij \rangle} T_{pa,ij} \left( p_i^\dagger a_j + p_j^\dagger a_i \right) \mathbf{r}_{ij}, \quad (17)$$

$$\mathbf{j}_{ap} = -\frac{ie}{\hbar} \sum_{\langle ij \rangle} T_{ap,ij} \left( a_i^\dagger p_j + a_j^\dagger p_i \right) \mathbf{r}_{ij}, \quad (18)$$

with  $\mathbf{r}_{ij} = \mathbf{r}_j - \mathbf{r}_i$ . We have replaced  $(|\mathbf{k}n\rangle, |\mathbf{k}m\rangle)$  by  $(|P\mathbf{k}n\rangle, |A\mathbf{k}m\rangle)$  to denote that these are Bloch states of the effective Hofstadter models for the parallel sector and anti-parallel sector respectively. Therefore,  $m, n$  now run over  $1, 2, \dots, L^2$  rather than upto  $2L^2$ . We have restricted the initial states to the parallel sector which is appropriate for our electron filling, and restricted the summation over intermediate states to just the anti-parallel bands since they are the dominant terms for the resonance. In the large  $J_H/t$  limit,  $|P\mathbf{k}n\rangle$  and  $|A\mathbf{k}m\rangle$  are annihilated by  $a$  and  $p$  operators respectively, which will be used below.

At this stage, we can integrate the imaginary part of the response from Eq. 16 to get

$$\mathcal{S} \approx \frac{\pi}{AJ_H} \sum_{\mathbf{k}mn} \text{Im} \mathcal{N}_{\mathbf{k}nm} \quad (19)$$

$$\mathcal{N}_{\mathbf{k}nm} = \langle P\mathbf{k}n | j_{pa}^x | A\mathbf{k}m \rangle \langle A\mathbf{k}m | j_{ap}^y | P\mathbf{k}n \rangle \quad (20)$$

As shown in Appendix A, the sum over  $m$  can be carried out exactly, which leads to the expectation value of a “kinetic energy”-type operators  $p_i^\dagger p_j$  in the state  $|P\mathbf{k}n\rangle$ . For a smooth, slowly varying skyrmion texture, the slow gradients of the spin direction are mainly captured by the prefactors  $T_{pa,ij}, T_{ap,ij}$ . The operator expectation values can be replaced, to leading order, by the corresponding expectation values in a uniform ferromagnet, which leads to the final result in Eq. 6.

To make progress on understanding the frequency dependence of the resonant Hall effect, we have examined the current matrix elements in the numerator of the Hall conductivity. For any fixed  $\mathbf{k}$ , our numerical calculation shows that  $|\langle P\mathbf{k}n | j_{pa}^x | A\mathbf{k}m \rangle \langle A\mathbf{k}m | j_{ap}^y | P\mathbf{k}n \rangle|$  has its largest magnitude around  $m \approx n$ , and it decays rapidly as  $|m - n|$  increases (see Appendix A for an illustrative plot of the matrix elements). The decay occurs over an energy window  $|(E_{\mathbf{k}m}^A - E_{\mathbf{k}n}^P) - J_H| < \alpha t$ , where  $\alpha \approx 1$  for  $R = 10$ . Since the matrix elements are peaked, while the denominator is a smooth function of the energy difference, it is a reasonable approximation to set

$$\sigma_{xy}^{\text{res}}(\omega) \approx -\frac{\hbar}{AJ_H} \frac{1}{\hbar\omega + i\tilde{\gamma} - J_H} \sum_{\mathbf{k}mn} \text{Im} \mathcal{N}_{\mathbf{k}nm} \quad (21)$$

where the effective broadening  $\tilde{\gamma} = \alpha t \ll J_H$  is determined by the energy window discussed above. This leads to the result in Eq.7, in agreement with the resonant Lorentzian response we find from our numerics. From

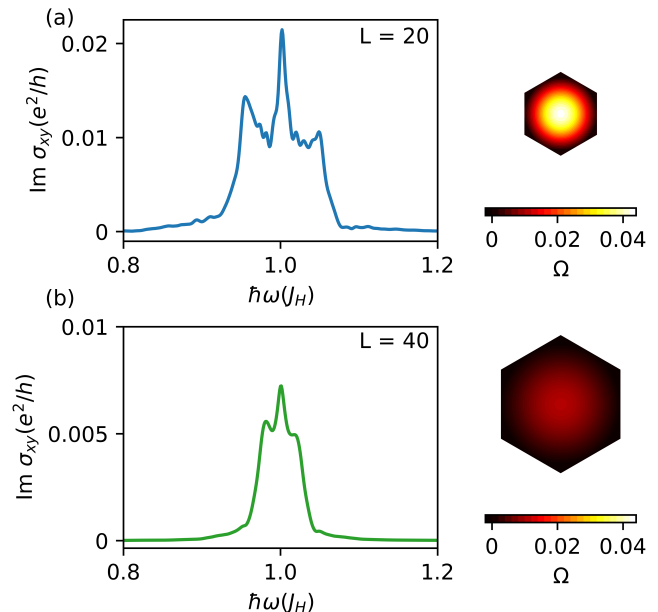


FIG. 6. Resonant feature in  $\text{Im} \sigma_{xy}$  for a skyrmion in a hexagonal box with (a) width  $L = 20$ , (b)  $L = 40$ . The color plots on the right show the profiles of the solid angle of the spin textures at each elementary plaquette, depicting a large real-space Berry phase gradient when  $L$  is small. We observe side peaks which move towards and merge with the main peak at  $J_H$  when  $L$  increases. For the larger  $L$ , the result has a stronger resemblance to the resonance in the SkX case. We attribute the side peaks to the inhomogeneity of the emergent magnetic field, as described in the text.

our numerical results, we also find that  $\tilde{\gamma}$  scales inversely with the unit cell width, roughly like  $1/L$ , so the resonant peak height of  $\text{Im} \sigma_{xy}^{\text{res}}$  scales roughly like the square root of the skyrmion density.

## V. HALL RESONANCE OF ISOLATED SKYRMION

To demonstrate that the resonance feature near  $J_H$  is present regardless of the crystal structure of the skyrmion spin texture, we consider the model  $H_0$  in an open-boundary hexagonal box of width  $L$ , as defined in Sec. II. The spin texture contains a single skyrmion of radius  $R = L/2$  centred in the middle of the box.

Figure 6 shows the corresponding  $\text{Im} \sigma_{xy}$  obtained from the real-space Kubo formula, demonstrating the presence of the resonance at  $J_H$  even with a single-skyrmion spin texture. The results are shown for a small and a large confinement area with  $L = 20$  and  $40$  respectively. The color plots to the right display the profile of the solid angle subtended by the three spins at each elementary triangular plaquette of the spin texture, a measure of the local scalar spin chirality, depicting a more gradual variation of the real-space Berry flux density (i.e., the emer-

gent magnetic field) in the larger box. We observe from these results that there is a central peak which agrees with the resonant feature seen in the SkX. In addition, we observe side peaks away from the main resonant peak at  $J_H$ ; these side peaks appear to merge into the resonant feature at  $J_H$  upon increasing the confinement area and the skyrmion size, thus better resembling the resonant peak of the SkX in Fig.4(a). We attribute these side peaks to the inhomogeneity of the emergent magnetic field of the skyrmion. We have found that when we cut out hexagonal unit cells centered at different points from the SkX spin texture in Sec.II, the side peaks become even more pronounced when the box is centered at the collinear regions where three skyrmions meet in Fig.1(a). In the collinear region, the emergent magnetic field is zero, whereas it becomes nonzero in the surrounding region which lies within the skyrmion core. This pattern of the emergent magnetic field resembles what has been studied in “magnetic anti-dot” structures, where the field is absent inside the dot region and nonzero outside. Such anti-dots support current-carrying localized states with a discrete energy-level spectrum [50–52]. The number of localized states trapped at the anti-dot and their degree of localization are enhanced when the field strength contrast between the inside and the outside is large, which occurs in our case when the real-space Berry phase gradient is big, namely small  $L$ . In our spinful electron model coupled to a spin texture, these energy levels appear in both the parallel and anti-parallel sectors. It is thus plausible that the observed side peaks originate from inter-sector transitions between these energy levels, which can occur at a frequency slightly different from  $J_H$ .

The persistence of the Hall resonance here implies that it is observable even when the texture is no longer a SkX, e.g. a disordered array of skyrmions. In fact, the resonance can be seen even in a minimal three-site system hosting a noncoplanar spin configuration, which will be studied next.

## VI. HALL RESONANCE IN A SPIN TRIMER

To illustrate the persistence of the Hall resonance in a minimal three-site system, we consider the following trimer model, analogous to Eq.1, defined on a triangular plaquette  $\Delta$  with three spins  $\{\mathbf{S}_i\}$  for  $i = 1, 2, 3 \in \Delta$  forming a non-zero solid angle  $\Omega_\Delta$ .

$$H_\Delta = -t \sum_{\langle ij \rangle \in \Delta} (c_{i\sigma}^\dagger c_{j\sigma} + h.c.) - J_H \sum_{i \in \Delta} \mathbf{s}_i \cdot \mathbf{S}_i. \quad (22)$$

For simplicity, we suppose that the three spins are related to one another by a  $2\pi/3$  rotation around the z-axis as the following.

$$\begin{aligned} \mathbf{S}_1 &= (\sin \theta \cos \varphi, \sin \theta \sin \varphi, \cos \theta), \\ \mathbf{S}_2 &= (\sin \theta \cos(\varphi + 2\pi/3), \sin \theta \sin(\varphi + 2\pi/3), \cos \theta), \\ \mathbf{S}_3 &= (\sin \theta \cos(\varphi + 4\pi/3), \sin \theta \sin(\varphi + 4\pi/3), \cos \theta), \end{aligned}$$

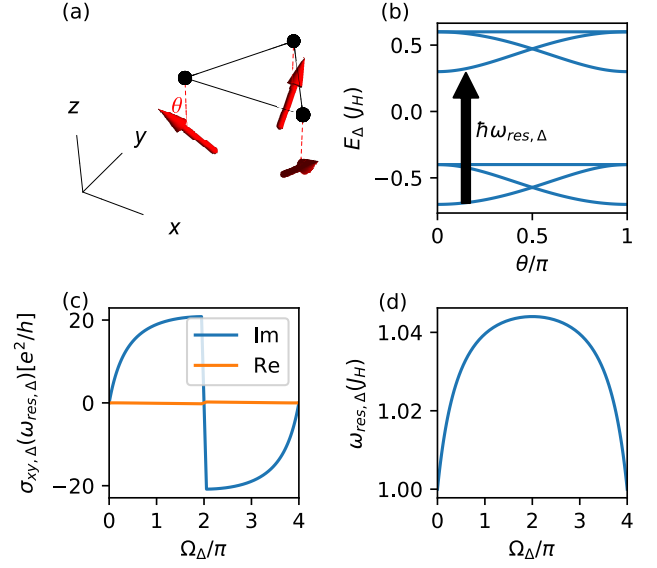


FIG. 7. (a) Schematic illustration of the trimer model. Red arrows denote the spin vectors on a triangular plaquette  $\Delta$  which form a noncoplanar spin configuration when the polar angle  $\theta$  is nonzero (mod  $\pi$ ). (b) Energy levels of trimer model as a function of  $\theta$  showing the presence of pairs of level whose energies differ by roughly  $J_H$ . This leads to a resonance in  $\sigma_{xy,\Delta}$  at  $\hbar\omega_{res,\Delta} \approx J_H$ . (c)  $\sigma_{xy,\Delta}$  at resonance as a function of the solid angle  $\Omega_\Delta$  subtended by the spins. (d) Small change in resonance frequency  $\omega_{res,\Delta}$  as a function of  $\Omega_\Delta$ .

where  $\theta \in [0, \pi]$  and  $\varphi = -\pi/6$ . This corresponds to the spin configuration in Fig.7(a). The model is invariant under the  $2\pi/3$  rotation, which admits an analytical expression for  $\sigma_{xy,\Delta}$  at resonance.

In the basis of  $\mathbf{C} = (c_{1\uparrow}, c_{1\downarrow}, c_{2\uparrow}, c_{2\downarrow}, c_{3\uparrow}, c_{3\downarrow})^T$ , the trimer model is represented by

$$\mathcal{H} = \mathcal{H}_0 + \mathcal{H}_1 + \mathcal{H}_2 + \mathcal{H}_3, \quad (23)$$

$$\mathcal{H}_0 = -t \begin{pmatrix} 0 & 1 & 1 \\ 1 & 0 & 1 \\ 1 & 1 & 0 \end{pmatrix} \otimes \mathbb{1}_{\text{spin}}, \quad (24)$$

$$\mathcal{H}_1 = -\frac{J_H}{2} \begin{pmatrix} 1 & 0 & 0 \\ 0 & 0 & 0 \\ 0 & 0 & 0 \end{pmatrix} \otimes \mathbf{S}_1 \cdot \boldsymbol{\sigma}, \quad (25)$$

$$\mathcal{H}_2 = -\frac{J_H}{2} \begin{pmatrix} 0 & 0 & 0 \\ 0 & 1 & 0 \\ 0 & 0 & 0 \end{pmatrix} \otimes \mathbf{S}_2 \cdot \boldsymbol{\sigma}, \quad (26)$$

$$\mathcal{H}_3 = -\frac{J_H}{2} \begin{pmatrix} 0 & 0 & 0 \\ 0 & 0 & 0 \\ 0 & 0 & 1 \end{pmatrix} \otimes \mathbf{S}_3 \cdot \boldsymbol{\sigma}. \quad (27)$$

$\mathcal{H}$  commutes with the three-fold rotational operator  $\mathcal{Z} =$

$\mathcal{W} \otimes \mathcal{U}$ , where  $\mathcal{W}$  and  $\mathcal{U}$  are expressed below.

$$\mathcal{W} = \begin{pmatrix} 0 & 0 & 1 \\ 1 & 0 & 0 \\ 0 & 1 & 0 \end{pmatrix}, \quad (28)$$

$$\mathcal{U} = \begin{pmatrix} e^{i\pi/3} & 0 \\ 0 & e^{-i\pi/3} \end{pmatrix}. \quad (29)$$

$\mathcal{W}$  has three eigenvalues  $\{1, \nu, \nu^2\}$ , where  $\nu = e^{i2\pi/3}$ , and the corresponding eigenvectors are given by

$$|\xi_1\rangle = \frac{1}{\sqrt{3}} (1 \ 1 \ 1)^T, \quad (30)$$

$$|\xi_\nu\rangle = \frac{1}{\sqrt{3}} (1 \ \nu^2 \ \nu)^T, \quad (31)$$

$$|\xi_{\nu^2}\rangle = \frac{1}{\sqrt{3}} (1 \ \nu \ \nu^2)^T, \quad (32)$$

respectively.  $\mathcal{U}$  has two eigenvalues  $\lambda = e^{i\pi/3}$  and  $\bar{\lambda} = e^{-i\pi/3}$  corresponding to the eigenvectors

$$|\chi_\lambda\rangle = (1 \ 0)^T, \quad (33)$$

$$|\chi_{\bar{\lambda}}\rangle = (0 \ 1)^T. \quad (34)$$

One can check that  $\mathcal{Z}$  has three eigenvalues  $\{-1, \lambda, \bar{\lambda}\}$ , each of which is two-fold degenerate. Denote the eigensubspaces of the three eigenvalues by  $\{|\psi_1\rangle, |\psi_2\rangle\}$ ,  $\{|\psi_3\rangle, |\psi_4\rangle\}$  and  $\{|\psi_5\rangle, |\psi_6\rangle\}$  respectively, where

$$|\psi_1\rangle = |\xi_\nu \otimes \chi_\lambda\rangle, \quad (35)$$

$$|\psi_2\rangle = |\xi_{\nu^2} \otimes \chi_{\bar{\lambda}}\rangle, \quad (36)$$

$$|\psi_3\rangle = |\xi_1 \otimes \chi_\lambda\rangle, \quad (37)$$

$$|\psi_4\rangle = |\xi_\nu \otimes \chi_{\bar{\lambda}}\rangle, \quad (38)$$

$$|\psi_5\rangle = |\xi_{\nu^2} \otimes \chi_\lambda\rangle, \quad (39)$$

$$|\psi_6\rangle = |\xi_1 \otimes \chi_{\bar{\lambda}}\rangle. \quad (40)$$

In the  $\{|\psi_a\rangle\}$  basis,  $\mathcal{H}$  is block diagonalized into three two-by-two blocks which can be further diagonalized straightforwardly. The spectrum of  $\mathcal{H}$  contains six energy levels as shown in Fig.7(b), featuring pairs of energy levels differing in energy by roughly  $J_H$ . At 1/6 filling, only the lowest level is occupied. At resonance  $\hbar\omega \approx J_H$ , the transition between the first and the fourth energy levels,  $E_1$  and  $E_4$ , is the only dominant contribution to the resonant peak  $\sigma_{xy,\Delta}^{\text{peak}}$ . For  $\theta \in [0, \pi/2)$ , these eigenstates are given by

$$|E_1\rangle = \frac{\zeta |\psi_3\rangle + \eta |\psi_4\rangle}{\sqrt{2}} \quad (41)$$

$$|E_4\rangle = \frac{\varrho |\psi_6\rangle + \kappa |\psi_5\rangle}{\sqrt{2}}, \quad (42)$$

$$E_1 = -\frac{t}{2} - \frac{1}{2} \sqrt{J_H^2 + 9t^2 + 6J_H t \cos \theta}, \quad (43)$$

$$E_4 = -\frac{t}{2} + \frac{1}{2} \sqrt{J_H^2 + 9t^2 - 6J_H t \cos \theta}, \quad (44)$$

where the coefficients  $\zeta, \eta, \varrho$  and  $\kappa$  are functions of  $t, J_H, \theta, \varphi$ .

$$\zeta = -\frac{\xi + J_H \cos \theta + 3t}{\sqrt{\xi(\xi + J_H \cos \theta + 3t)}}, \quad (45)$$

$$\eta = -\frac{J_H \sin \theta e^{i\varphi}}{\sqrt{\xi(\xi + J_H \cos \theta + 3t)}}, \quad (46)$$

$$\varrho = \frac{\xi' + J_H \cos \theta - 3t}{\sqrt{\xi'(\xi' + J_H \cos \theta - 3t)}}, \quad (47)$$

$$\kappa = -\frac{J_H \sin \theta e^{-i\varphi}}{\sqrt{\xi'(\xi' + J_H \cos \theta - 3t)}}, \quad (48)$$

$$\xi = \sqrt{J_H^2 + 9t^2 + 6J_H t \cos \theta}, \quad (49)$$

$$\xi' = \sqrt{J_H^2 + 9t^2 - 6J_H t \cos \theta}. \quad (50)$$

Using these eigenfunctions to compute the resonant peak  $\sigma_{xy,\Delta}^{\text{peak}}$  and keeping only the interlevel contribution between  $|E_1\rangle$  and  $|E_4\rangle$ , we obtain

$$\sigma_{xy,\Delta}^{\text{peak}} \approx \frac{i\sqrt{3}t^2}{4\hbar\omega_{\text{res},\Delta}\gamma} \frac{e^2}{\hbar} |\zeta^* \kappa - \varrho \eta^*|^2, \quad (51)$$

where  $\hbar\omega_{\text{res},\Delta} = E_4 - E_1$  changes slightly with  $\theta$  and is plotted as a function of  $\Omega_\Delta$  in Fig.7(d). The term  $|\zeta^* \kappa - \varrho \eta^*|^2$  depends on  $\theta$  as  $\sim \sin^2 \theta$  peaking as  $\theta$  approaches  $\pi/2$  from below, in agreement with the monotonic increasing of  $\text{Im} \sigma_{xy,\Delta}^{\text{peak}}$  with  $\Omega_\Delta$ , as shown in Fig.7(c), for  $\Omega_\Delta \in [0, 2\pi)$ . While crossing from  $\theta \in [0, \pi/2)$  to  $(\pi/2, \pi]$ , the energy levels can cross one another as shown in Fig.7(b).  $\text{Im} \sigma_{xy,\Delta}^{\text{peak}}$  switches sign abruptly and scales with  $\theta$  like  $\sim -\sin^2 \theta$  instead, which can be confirmed by recalculating Eq.51 taking into account the level crossing. The sharp jump at  $(\theta, \Omega_\Delta) = (\pi/2, 2\pi)$  is expected to be smoothed out by thermal broadening as the temperature rises. We have also checked that the analytical expression agrees very well with the numerical results which incorporate other less dominant inter-level contributions to Hall conductivity, i.e. the transition involving  $|E_1\rangle$  and  $|E_a\rangle$  for  $a \neq 1, 4$ . Our key observation is that  $\text{Im} \sigma_{xy,\Delta}^{\text{peak}}$  grows monotonically with the solid angle  $\Omega_\Delta$ , at least for small  $\Omega_\Delta$ . An implication of this finding is that the Hall resonance can be utilized in a local optical probe which can distinguish regions with spin noncoplanarity from those without the noncoplanarity, thereby enabling a visualization of a spin texture hosting skyrmions and perhaps other noncoplanar magnetic objects.

Before concluding the section, we examine a possible connection for a given spin texture between the net Hall response and the local Hall response  $\sigma_{xy,\Delta}$  associated with a local  $\Omega_\Delta$ . Under a high-frequency applied electric field, the electronic response is expected to be local. That is, in an inhomogeneous system, the overall response function can be approximated by the local response function associated with the local property, that exhibits the inhomogeneity, averaged over the system, e.g. magnetization in inhomogeneous magnetic domain

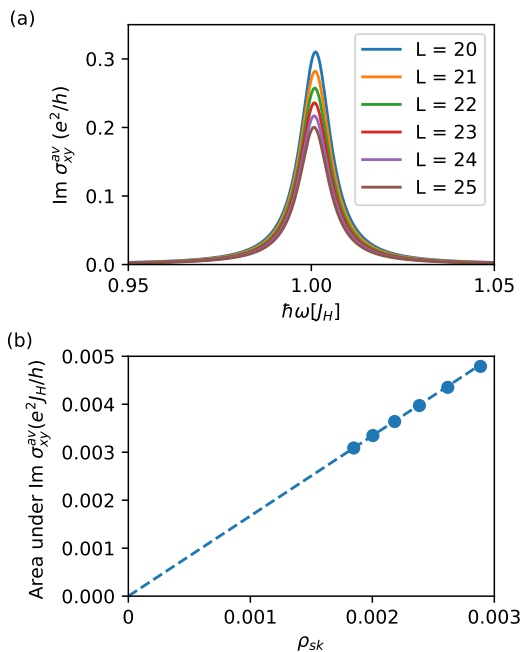


FIG. 8. Results from the local approximation: (a) Lorentzian-like resonance of  $\text{Im } \sigma_{xy}^{\text{av}}$  near  $\hbar\omega = J_H$  for various SkX's with different skyrmion densities  $\rho_{sk} = 2/\sqrt{3}L^2$ . (b) A linear relation between  $\rho_{sk}$  and the area under  $\text{Im } \sigma_{xy}^{\text{av}}(\omega)$  in (a).

configuration [37] or the real-space Berry phase associated with  $\Omega_\Delta$  in the case of skyrmion spin texture. A supporting argument for this is to regard the electrons as semi-classical objects which traverse only a small distance after several cycles of the high-frequency applied field, thereby sensing only the local properties [37] [53]. For a given skyrmion spin texture, the Hall conductivity obtained from averaging the local Hall conductivity is given by

$$\sigma_{xy}^{\text{av}} = \frac{1}{N_\Delta} \sum_{\Delta} \sigma_{xy,\Delta}, \quad (52)$$

where the local Hall response  $\sigma_{xy,\Delta}$  can be computed using the trimer model,  $N_\Delta$  is the number of the plaquette, and the sum is carried over all the triangular plaquettes.

Figure 8(a) shows the frequency dependence of  $\text{Im } \sigma_{xy}^{\text{av}}$  featuring a resonance near  $J_H$  for a series of SkX studied in Sec.III C. We observe a very sharp resonance whose height is an order of magnitude higher than that in Fig.5(a), whereas the resonance width is an order of magnitude smaller. This is the consequence of having an enormous amount of nearly degenerate atomic-like energy levels due to the absence of the inter-trimer hopping. The hopping is expected to lift the degeneracy, which permits other transition channels at frequencies different from  $J_H$ , thereby broadening the resonance width to resemble Fig.5(a) better. Figure 8(b) shows the scaling between the area under the resonance and  $\rho_{sk}$ , which exhibits a linear relation identical to Fig.5(b), except that

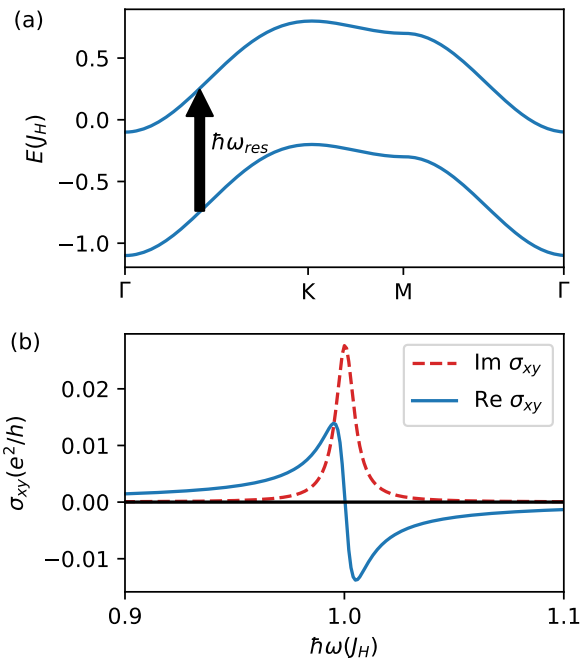


FIG. 9. (a) Band structure of the model with Rashba SOC,  $H_0 + H_R$ , for a ferromagnetic spin texture  $\mathbf{S}_i = \hat{z}$ , featuring similarly dispersing bands differing in energy by approximately  $J_H$ . (b) A resonance feature near  $\hbar\omega = J_H$  arises from the Rashba SOC and the similarly dispersing bands.

the values are three times larger. We attribute this overestimate to the fact that the electrons are highly confined to each plaquette, which provides a better chance for the inter-sector transitions to occur compared with when the electrons are more delocalized in a lattice environment. Therefore, maintaining a certain degree of delocalization by enlarging the number of sites beyond the trimer is a promising way to reduce the discrepancy between the local approximation and the actual results.

## VII. IMPACT OF SPIN-ORBIT COUPLING

So far, the effect of spin-orbit coupling (SOC) has been ignored. SOC, like skyrmion, can also produce a resonance in Hall conductivity near  $\hbar\omega = J_H$ , which can already be seen even in a simple ferromagnetic spin texture. To demonstrate this, we introduce a Rashba hopping term  $H_R$ , defined below, into Eq.1 and set  $\mathbf{S}_i = \hat{z}$ .

$$H_R = - \sum_{\langle ij \rangle} i\chi_R c_{i\alpha}^\dagger (\hat{z} \times \hat{\mathbf{r}}_{ij} \cdot \boldsymbol{\sigma}_{\alpha\beta}) c_{j\beta} + h.c., \quad (53)$$

where  $\hat{\mathbf{r}}_{ij}$  is the unit vector of  $\mathbf{r}_{ij} = \mathbf{r}_j - \mathbf{r}_i$ , and  $\chi_R$  is the strength of the Rashba SOC. Figure 9(a) shows the band structure of  $H_0 + H_R$  for  $\chi_R = 0.05t$ , featuring similarly dispersing bands differing in energy by roughly  $J_H$ . As a result, a resonant feature is obtained near  $J_H$ , as shown in Fig.9(b) in the same frequency window as that

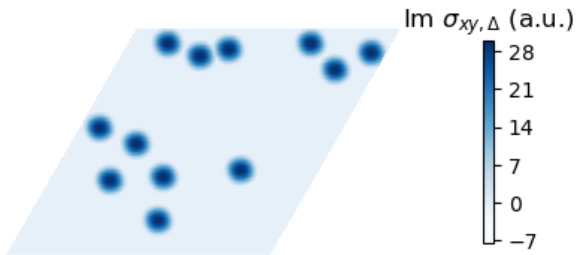


FIG. 10. Real-space profile of  $\text{Im } \sigma_{xy,\Delta}$  for a random skyrmion array at resonance  $\hbar\omega \approx J_H$  obtained from the local approximation. The dark droplets corresponding to a large nonzero-frequency topological Hall conductivity are the skyrmions, while the bright regions with  $\text{Im } \sigma_{xy,\Delta} = 0$  correspond to the ferromagnetic background. The color scale in this spatial map is in arbitrary units since the value of  $\text{Im } \sigma_{xy,\Delta}$  is sensitive to the broadening  $\gamma$ . Such a profile could potentially be mapped out by magneto-optical Kerr microscopy which is known to probe the local Hall conductivity, enabling the resonant optical Hall conductivity as a tool to visualize skyrmions.

for skyrmion spin textures. When the texture contains skyrmions, we also expect SOC to generate a resonance at  $J_H$ , and experiments will detect the effect of both. Recent works on d.c. Hall effect have made it increasingly apparent that SOC and non-collinearity of a spin texture intertwine to produce a resultant Hall effect which is not simply the addition of the individual contributions, so  $\sigma_{xy} \neq \sigma_{xy}^{\text{soc}} + \sigma_{xy}^{\text{skx}}$  [54–56]. For instance, there can be extra Hall effect contributions arising only in the simultaneous presence of SOC and the non-collinearity [54, 56]. It is very likely that the intertwined effect also appears in the non-zero-frequency Hall effect; therefore, a study where skyrmion spin texture and SOC are simultaneously treated is generally needed to make a *quantitative* comparison with experiments. This is left for the future. Even so, based on our results in the previous section, we expect the presence of skyrmions to be detectable using optical Hall measurements since it gives rise to a distinct optical Hall response between a spin texture containing skyrmions and other ordered phases, e.g. ferromagnetic order. Such a difference is expected to be pronounced when the skyrmion density is large.

### VIII. CONCLUSION

We have shown that in a 2D model of conduction electrons coupled to skyrmion spin textures via a Hund’s

coupling, a high-frequency resonance in Hall conductivity arises at a characteristic frequency set by the Hund’s coupling. For SkX spin textures, the resonance originates from transitions between many pairs of topological Chern bands which disperse similarly and differ in energy by a similar amount  $\approx J_H$ . Its presence does not depend on whether the spin texture is a crystal of skyrmions or a single skyrmion. A linear relation between the skyrmion density and the area under the Hall resonance,  $\text{Im } \sigma_{xy}(\omega)$ , is found and is explained using a smooth texture approximation and a local approximation. Probes such as the magneto-optical Kerr effect and Faraday effect, which are known to track non-zero-frequency Hall conductivity, may be suitable experimental techniques for detecting the optical topological Hall conductivity and its resonance. Near the resonant frequency, a real-space profile of a skyrmion spin texture may be mapped out using Kerr microscopy technique, as theoretically shown in Fig.10. Our results can be tested in materials hosting a large density of skyrmions such as  $\text{Gd}_2\text{PdSi}_3$  [18],  $\text{Gd}_3\text{Ru}_4\text{Al}_{12}$  [19],  $\text{GdRu}_2\text{Si}_2$  [20], and  $\text{MnGe}$  [12]. We also point out how SOC can produce a similar resonance and how it affects the experimental manifestation of the resonant topological Hall conductivity. Similar to the d.c. Hall effect [54, 56], a *quantitative* comparison with experiments when skyrmions and significant SOC coexist generally requires a study where both skyrmions and SOC are simultaneously treated. Studying this would be the next logical step in exploring optical probes of skyrmions. It is also intriguing to explore whether the Hall resonance, involving pairs of topological Chern bands, can be understood using the state-pairwise geometrical construction formulated in Ref.[57].

### ACKNOWLEDGMENTS

We thank Michael Bartram for a related collaboration and discussions. This work was funded by NSERC of Canada. This research was enabled in part by support provided by WestGrid ([www.westgrid.ca](http://www.westgrid.ca)) and Compute Canada Calcul Canada ([www.computecanada.ca](http://www.computecanada.ca)).

[1] T. Skyrme, A unified field theory of mesons and baryons, *Nuclear Physics* **31**, 556 (1962).

[2] N. Nagaosa and Y. Tokura, Topological properties and dynamics of magnetic skyrmions, *Nature Nanotechnology* **8**, 899 (2013).

- [3] A. Fert, V. Cros, and J. Sampaio, Skyrmions on the track, *Nature Nanotechnology* **8**, 152 (2013).
- [4] W. Jiang, G. Chen, K. Liu, J. Zang, S. G. te Velthuis, and A. Hoffmann, Skyrmions in magnetic multilayers, *Physics Reports* **704**, 1 (2017), skyrmions in Magnetic Multilayers.
- [5] C. Back, V. Cros, H. Ebert, K. Everschor-Sitte, A. Fert, M. Garst, T. Ma, S. Mankovsky, T. L. Monchesky, M. Mostovoy, N. Nagaosa, S. S. P. Parkin, C. Pfleiderer, N. Reyren, A. Rosch, Y. Taguchi, Y. Tokura, K. von Bergmann, and J. Zang, The 2020 skyrmionics roadmap, *Journal of Physics D: Applied Physics* **53**, 363001 (2020).
- [6] Y. Tokura and N. Kanazawa, Magnetic skyrmion materials, *Chemical Reviews* **121**, 2857 (2021).
- [7] S. E. Barrett, G. Dabbagh, L. N. Pfeiffer, K. W. West, and R. Tycko, Optically pumped nmr evidence for finite-size skyrmions in gaas quantum wells near landau level filling  $\nu = 1$ , *Phys. Rev. Lett.* **74**, 5112 (1995).
- [8] Y. P. Shkolnikov, S. Misra, N. C. Bishop, E. P. De Poortere, and M. Shayegan, Observation of quantum hall “valley skyrmions”, *Phys. Rev. Lett.* **95**, 066809 (2005).
- [9] A. Neubauer, C. Pfleiderer, B. Binz, A. Rosch, R. Ritz, P. G. Niklowitz, and P. Böni, Topological hall effect in the  $a$  phase of mnsi, *Phys. Rev. Lett.* **102**, 186602 (2009).
- [10] M. Lee, W. Kang, Y. Onose, Y. Tokura, and N. P. Ong, Unusual hall effect anomaly in mnsi under pressure, *Phys. Rev. Lett.* **102**, 186601 (2009).
- [11] S. Mühlbauer, B. Binz, F. Jonietz, C. Pfleiderer, A. Rosch, A. Neubauer, R. Georgii, and P. Böni, Skyrmion lattice in a chiral magnet, *Science* **323**, 915 (2009).
- [12] N. Kanazawa, J.-H. Kim, D. S. Inosov, J. S. White, N. Egetenmeyer, J. L. Gavilano, S. Ishiwata, Y. Onose, T. Arima, B. Keimer, and Y. Tokura, Possible skyrmion-lattice ground state in the  $b20$  chiral-lattice magnet mnge as seen via small-angle neutron scattering, *Phys. Rev. B* **86**, 134425 (2012).
- [13] X. Z. Yu, Y. Onose, N. Kanazawa, J. H. Park, J. H. Han, Y. Matsui, N. Nagaosa, and Y. Tokura, Real-space observation of a two-dimensional skyrmion crystal, *Nature* **465**, 901 (2010).
- [14] S. Seki, X. Z. Yu, S. Ishiwata, and Y. Tokura, Observation of skyrmions in a multiferroic material, *Science* **336**, 198 (2012).
- [15] C. Moreau-Luchaire, C. Moutafis, N. Reyren, J. Sampaio, C. A. F. Vaz, N. Van Horne, K. Bouzehouane, K. Garcia, C. Deranlot, P. Warnicke, P. Wohlhüter, J.-M. George, M. Weigand, J. Raabe, V. Cros, and A. Fert, Additive interfacial chiral interaction in multilayers for stabilization of small individual skyrmions at room temperature, *Nature Nanotechnology* **11**, 444 (2016).
- [16] L. Wang, Q. Feng, Y. Kim, R. Kim, K. H. Lee, S. D. Pollard, Y. J. Shin, H. Zhou, W. Peng, D. Lee, W. Meng, H. Yang, J. H. Han, M. Kim, Q. Lu, and T. W. Noh, Ferroelectrically tunable magnetic skyrmions in ultrathin oxide heterostructures, *Nature Materials* **17**, 1087 (2018).
- [17] T. Okubo, S. Chung, and H. Kawamura, Multiple- $q$  states and the skyrmion lattice of the triangular-lattice heisenberg antiferromagnet under magnetic fields, *Phys. Rev. Lett.* **108**, 017206 (2012).
- [18] T. Kurumaji, T. Nakajima, M. Hirschberger, A. Kikkawa, Y. Yamasaki, H. Sagayama, H. Nakao, Y. Taguchi, T.-h. Arima, and Y. Tokura, Skyrmion lattice with a giant topological hall effect in a frustrated triangular-lattice magnet, *Science* **365**, 914 (2019).
- [19] M. Hirschberger, T. Nakajima, S. Gao, L. Peng, A. Kikkawa, T. Kurumaji, M. Kriener, Y. Yamasaki, H. Sagayama, H. Nakao, K. Ohishi, K. Kakurai, Y. Taguchi, X. Yu, T.-h. Arima, and Y. Tokura, Skyrmion phase and competing magnetic orders on a breathing kagomé lattice, *Nature Communications* **10**, 5831 (2019).
- [20] N. D. Khanh, T. Nakajima, X. Yu, S. Gao, K. Shibata, M. Hirschberger, Y. Yamasaki, H. Sagayama, H. Nakao, L. Peng, K. Nakajima, R. Takagi, T.-h. Arima, Y. Tokura, and S. Seki, Nanometric square skyrmion lattice in a centrosymmetric tetragonal magnet, *Nature Nanotechnology* **15**, 444 (2020).
- [21] A. Wugalter, Y. Komijani, and P. Coleman, Large- $n$  approach to the two-channel kondo lattice, *Phys. Rev. B* **101**, 075133 (2020).
- [22] M. Kornjača, V. L. Quito, and R. Flint, Mobile majorana zero-modes in two-channel kondo insulators, arXiv preprint arXiv:2104.11173 (2021).
- [23] E. Khalaf, S. Chatterjee, N. Bultinck, M. P. Zaletel, and A. Vishwanath, Charged skyrmions and topological origin of superconductivity in magic-angle graphene, *Science Advances* **7** (2021), 10.1126/sciadv.abf5299.
- [24] A. Soumyanarayanan, M. Raju, A. L. Gonzalez Oyarce, A. K. C. Tan, M.-Y. Im, A. P. Petrović, P. Ho, K. H. Khoo, M. Tran, C. K. Gan, F. Ernult, and C. Panagopoulos, Tunable room-temperature magnetic skyrmions in ir/fe/co/pt multilayers, *Nature Materials* **16**, 898 (2017).
- [25] D. Maccariello, W. Legrand, N. Reyren, K. Garcia, K. Bouzehouane, S. Collin, V. Cros, and A. Fert, Electrical detection of single magnetic skyrmions in metallic multilayers at room temperature, *Nature Nanotechnology* **13**, 233 (2018).
- [26] X. Z. Yu, N. Kanazawa, Y. Onose, K. Kimoto, W. Z. Zhang, S. Ishiwata, Y. Matsui, and Y. Tokura, Near room-temperature formation of a skyrmion crystal in thin-films of the helimagnet fege, *Nature Materials* **10**, 106 (2011).
- [27] J. Ye, Y. B. Kim, A. J. Millis, B. I. Shraiman, P. Majumdar, and Z. Tešanović, Berry phase theory of the anomalous hall effect: Application to colossal magnetoresistance manganites, *Phys. Rev. Lett.* **83**, 3737 (1999).
- [28] T. Schulz, R. Ritz, A. Bauer, M. Halder, M. Wagner, C. Franz, C. Pfleiderer, K. Everschor, M. Garst, and A. Rosch, Emergent electrodynamics of skyrmions in a chiral magnet, *Nature Physics* **8**, 301 (2012).
- [29] Y. Shiomi, N. Kanazawa, K. Shibata, Y. Onose, and Y. Tokura, Topological nernst effect in a three-dimensional skyrmion-lattice phase, *Phys. Rev. B* **88**, 064409 (2013).
- [30] M. Hirschberger, L. Spitz, T. Nomoto, T. Kurumaji, S. Gao, J. Masell, T. Nakajima, A. Kikkawa, Y. Yamasaki, H. Sagayama, H. Nakao, Y. Taguchi, R. Arita, T.-h. Arima, and Y. Tokura, Topological nernst effect of the two-dimensional skyrmion lattice, *Phys. Rev. Lett.* **125**, 076602 (2020).
- [31] S. K. Kim, K. Nakata, D. Loss, and Y. Tserkovnyak, Tunable magnonic thermal hall effect in skyrmion crystal phases of ferrimagnets, *Phys. Rev. Lett.* **122**, 057204 (2019).

- [32] D. Kan, T. Moriyama, K. Kobayashi, and Y. Shimakawa, Alternative to the topological interpretation of the transverse resistivity anomalies in  $\text{SrRuO}_3$ , *Phys. Rev. B* **98**, 180408 (2018).
- [33] A. Gerber, Interpretation of experimental evidence of the topological hall effect, *Phys. Rev. B* **98**, 214440 (2018).
- [34] L. Wang, Q. Feng, H. G. Lee, E. K. Ko, Q. Lu, and T. W. Noh, Controllable thickness inhomogeneity and berry curvature engineering of anomalous hall effect in  $\text{SrRuO}_3$  ultrathin films, *Nano Letters* **20**, 2468 (2020).
- [35] G. Kim, K. Son, Y. E. Suyolcu, L. Miao, N. J. Schreiber, H. P. Nair, D. Putzky, M. Minola, G. Christiani, P. A. van Aken, K. M. Shen, D. G. Schlom, G. Logvenov, and B. Keimer, Inhomogeneous ferromagnetism mimics signatures of the topological hall effect in  $\text{SrRuO}_3$  films, *Phys. Rev. Materials* **4**, 104410 (2020).
- [36] L. Wu, F. Wen, Y. Fu, J. H. Wilson, X. Liu, Y. Zhang, D. M. Vasiukov, M. S. Kareev, J. H. Pixley, and J. Chakhalian, Berry phase manipulation in ultrathin  $\text{SrRuO}_3$  films, *Phys. Rev. B* **102**, 220406 (2020).
- [37] F. M. Bartram, S. Sorn, Z. Li, K. Hwangbo, S. Shen, F. Frontini, L. He, P. Yu, A. Paramakanti, and L. Yang, Anomalous kerr effect in  $\text{SrRuO}_3$  thin films, *Phys. Rev. B* **102**, 140408 (2020).
- [38] S. Sorn and A. Paramakanti, Domain wall skew scattering in ferromagnetic weyl metals, *Phys. Rev. B* **103**, 104413 (2021).
- [39] P. W. Anderson and H. Hasegawa, Considerations on double exchange, *Phys. Rev.* **100**, 675 (1955).
- [40] K. Ohgushi, S. Murakami, and N. Nagaosa, Spin anisotropy and quantum hall effect in the kagomé lattice: Chiral spin state based on a ferromagnet, *Phys. Rev. B* **62**, R6065 (2000).
- [41] K. Hamamoto, M. Ezawa, and N. Nagaosa, Quantized topological hall effect in skyrmion crystal, *Phys. Rev. B* **92**, 115417 (2015).
- [42] S. Banerjee, J. Rowland, O. Erten, and M. Randeria, Enhanced stability of skyrmions in two-dimensional chiral magnets with rashba spin-orbit coupling, *Phys. Rev. X* **4**, 031045 (2014).
- [43] D. R. Hofstadter, Energy levels and wave functions of bloch electrons in rational and irrational magnetic fields, *Phys. Rev. B* **14**, 2239 (1976).
- [44] B. Göbel, A. Mook, J. Henk, and I. Mertig, Unconventional topological hall effect in skyrmion crystals caused by the topology of the lattice, *Phys. Rev. B* **95**, 094413 (2017).
- [45] B. Göbel, A. Mook, J. Henk, and I. Mertig, The family of topological hall effects for electrons in skyrmion crystals, *The European Physical Journal B* **91**, 179 (2018).
- [46] S. Sorn, S. Divic, and A. Paramakanti, Tunable skyrmion crystals and topological quantum oscillations in magnetic metals, *Phys. Rev. B* **100**, 174411 (2019).
- [47] G. Mahan, *Many-Particle Physics*, Physics of Solids and Liquids (Springer US, 2000).
- [48] P. Coleman, *Introduction to many-body physics* (Cambridge University Press, 2015).
- [49] D. Tong, Lectures on the quantum hall effect, arXiv preprint arXiv:1606.06687 (2016).
- [50] H.-S. Sim, K.-H. Ahn, K. J. Chang, G. Ihm, N. Kim, and S. J. Lee, Magnetic edge states in a magnetic quantum dot, *Phys. Rev. Lett.* **80**, 1501 (1998).
- [51] J. Reijniers, F. M. Peeters, and A. Matulis, Quantum states in a magnetic antidot, *Phys. Rev. B* **59**, 2817 (1999).
- [52] A. Kormányos, P. Rakyta, L. Oroszlány, and J. Cserti, Bound states in inhomogeneous magnetic field in graphene: Semiclassical approach, *Phys. Rev. B* **78**, 045430 (2008).
- [53] This statement depends on a few variables including the actual frequency of the applied field, the electron group velocity, and the degree of inhomogeneity in the system. A sufficient condition is that the distance travelled by the electron in a few cycles is small compared with the length scale characterizing the variation of the inhomogeneity, e.g. periodicity  $L$  in the case of a SkX.
- [54] F. R. Lux, F. Freimuth, S. Blügel, and Y. Mokrousov, Chiral hall effect in noncollinear magnets from a cyclic cohomology approach, *Phys. Rev. Lett.* **124**, 096602 (2020).
- [55] S.-S. Zhang, H. Ishizuka, H. Zhang, G. B. Halász, and C. D. Batista, Real-space berry curvature of itinerant electron systems with spin-orbit interaction, *Phys. Rev. B* **101**, 024420 (2020).
- [56] J. Bouaziz, H. Ishida, S. Lounis, and S. Blügel, Transverse transport in two-dimensional relativistic systems with nontrivial spin textures, *Phys. Rev. Lett.* **126**, 147203 (2021).
- [57] J. Ahn, G.-Y. Guo, N. Nagaosa, and A. Vishwanath, Riemannian geometry of resonant optical responses, arXiv preprint arXiv:2103.01241 (2021).

## Appendix A: Simplifying the Kubo formula for sum rule and resonant Hall conductivity

In this appendix, we will show that the area under the resonance of  $\text{Im } \sigma_{xy}$ ,  $\mathcal{S}$ , is proportional to  $\rho_{sk}$ .

$$\begin{aligned} \mathcal{S} &= \int d\omega \text{Im } \sigma_{xy}^{\text{res}}(\omega), \\ &\approx \frac{\pi}{\mathcal{A}J_H} \text{Im} \sum_{\mathbf{k}} \sum_{E_{\mathbf{k}n}^P < \mu} \sum_m \langle P\mathbf{k}n | j_{pa}^x | A\mathbf{k}m \rangle \langle A\mathbf{k}m | j_{ap}^y | P\mathbf{k}n \rangle, \end{aligned} \quad (\text{A1})$$

$$\equiv \frac{\pi}{\mathcal{A}J_H} \text{Im } \mathcal{N}. \quad (\text{A2})$$

The magnitude of the matrix element  $\langle P\mathbf{k}n | j_{pa}^x | A\mathbf{k}m \rangle \langle A\mathbf{k}m | j_{ap}^y | P\mathbf{k}n \rangle$  is found to generally peak around  $n \approx m$ , and it decays abruptly as  $|n - m|$  increases, as illustrated by Fig.11. This sharp feature is used to shed light on the

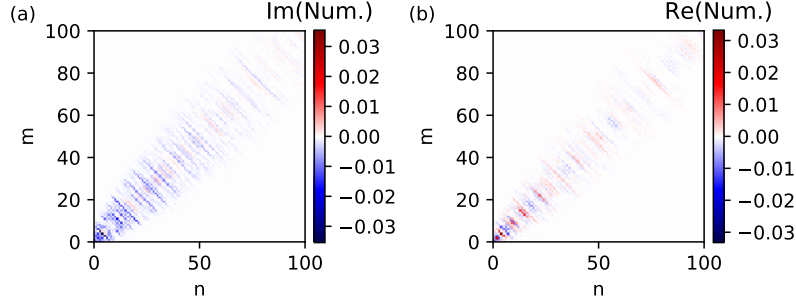


FIG. 11. Color plots illustrating that the numerator in the Kubo formula in Eq.16, involving current operator matrix elements, has its magnitude peaking around  $n = m$  and decaying quickly with increasing  $|n - m|$ . The result is obtained at a generic crystal momentum  $\mathbf{k}$  and for  $L = 20$ .

Lorentzian shape of the Hall resonance in the main text. The Hall resonance curve  $\sigma_{xy}^{\text{res}}(\omega)$  in Eq.7 and the area  $\mathcal{S}$  above can be obtained by calculating  $\mathcal{N}$ , which can be simplified by the following observations.

Observation (1): we can use the Bloch theorem to convert the matrix elements of  $j_{pa}^x$  and  $j_{ap}^y$ , which involve the whole lattice summation, into summations over a chosen magnetic unit cell, i.e.

$$\langle P\mathbf{k}n | j_{pa}^x | A\mathbf{k}m \rangle = -\frac{ieN_{sk}}{\hbar} \sum_{i \in u.c.} \sum_{\delta_a} T_{pa, i(i+\delta_a)} \langle P\mathbf{k}n | p_i^\dagger a_{i+\delta_a} + p_{i+\delta_a}^\dagger a_i | A\mathbf{k}m \rangle \delta_{a,x}, \quad (\text{A3})$$

$$\langle A\mathbf{k}m | j_{ap}^y | P\mathbf{k}n \rangle = -\frac{ieN_{sk}}{\hbar} \sum_{i \in u.c.} \sum_{\delta_a} T_{ap, i(i+\delta_a)} \langle A\mathbf{k}m | a_i^\dagger p_{i+\delta_a} + a_{i+\delta_a}^\dagger p_i | P\mathbf{k}n \rangle \delta_{a,y}, \quad (\text{A4})$$

where  $N_{sk}$  denotes the number of skyrmion in the system which equals to the number of unit cell since we have one skyrmion per unit cell.  $\delta_a$  are the nearest neighbor vectors.

$$\delta_1 = (1, 0), \quad (\text{A5})$$

$$\delta_2 = (1/2, \sqrt{3}/2), \quad (\text{A6})$$

$$\delta_3 = (-1/2, \sqrt{3}/2). \quad (\text{A7})$$

Observation (2): the operator  $\sum_m |A\mathbf{k}m\rangle \langle A\mathbf{k}m|$  can be shown to be diagonal in the sublattice index  $s$ .

$$\sum_m |A\mathbf{k}m\rangle \langle A\mathbf{k}m| = \sum_{\mathbf{D}, \mathbf{D}', s} \frac{e^{i\mathbf{k} \cdot (\mathbf{D} - \mathbf{D}')}}{N_{sk}} |A\mathbf{D}s\rangle \langle A\mathbf{D}'s| \quad (\text{A8})$$

where  $s = 1, \dots, L^2$  is the sublattice index,  $|A\mathbf{D}s\rangle$  is an anti-parallel electron state localized at a site whose position is given by  $\mathbf{D} + \mathbf{d}_s$ , where  $\mathbf{D}$  is the position of a reference point of a unit cell, and  $\mathbf{d}_s$  is the position of the site relative to the reference point. When this is used concurrently with observation (1), the phase factor becomes unity as the unit cell is fixed to be the same for the matrix elements of  $j_{pa}^x$  and  $j_{ap}^y$ .

For a given bond  $\langle i(i + \delta_a) \rangle$  in the  $j_{pa}^x$  matrix element, the  $s$ -diagonal feature selects only several bonds  $\langle i(i + \delta_a) \rangle$ 's in  $j_{ap}^y$  matrix element. Suppose that  $\langle i_1 i_2 \rangle$  and  $\langle i_3 i_4 \rangle$  are the relevant bonds from  $j_{pa}^x$  and  $j_{ap}^y$  respectively, the contribution to  $\mathcal{N}$  becomes  $\sim \langle P\mathbf{k}n | (p_{i_1}^\dagger a_{i_2} + p_{i_2}^\dagger a_{i_1}) (a_{i_3}^\dagger p_{i_4} + a_{i_4}^\dagger p_{i_3}) | P\mathbf{k}n \rangle = \langle P\mathbf{k}n | p_{i_5}^\dagger p_{i_6} | P\mathbf{k}n \rangle$ , where  $i_5$  and  $i_6$  are two sites taken from  $\{i_1, i_2, i_3, i_4\}$ , and the precise answer depends on the type of bonds, which will be illustrated later. To arrive at this property, we recall that  $a$  and  $p$  operator annihilate  $|P\mathbf{k}n\rangle$  and  $|A\mathbf{k}m\rangle$  respectively.

From these,  $\mathcal{N}$  becomes

$$\mathcal{N} = N_{sk} \left( \frac{ie}{\hbar} \right)^2 \sum_{\mathbf{k}} \sum_{E_{\mathbf{k}n}^P < \mu} \sum_{\langle i_1 i_2 \rangle} \sum_{\langle i_3 i_4 \rangle} \langle P\mathbf{k}n | Q_{i_1 i_2 i_3 i_4}^{i_5 i_6} | P\mathbf{k}n \rangle, \quad (\text{A9})$$

$$Q_{i_1 i_2 i_3 i_4}^{i_5 i_6} = T_{pa, i_1 i_2} T_{ap, i_3 i_4} \mathbf{r}_{i_1 i_2, x} \mathbf{r}_{i_3 i_4, y} p_{i_5}^\dagger p_{i_6}, \quad (\text{A10})$$

where the sum over  $\langle i_1 i_2 \rangle$  is the equivalence of  $\sum_{i_1 \in u.c.} \sum_{\delta_a}$  with  $i_2 = i_1 + \delta_a$ . The sum over  $\langle i_3 i_4 \rangle$  is similarly defined, except that it is done over a more restricted subset as mentioned earlier, and hence the double prime. There are three types of  $\langle i_1 i_2 \rangle$  bond associated with the nearest neighbor vectors. However, there are only two types of  $\langle i_3 i_4 \rangle$  associated with  $\delta_2$  and  $\delta_3$  since  $\delta_1$  has a vanishing  $y$ -component.

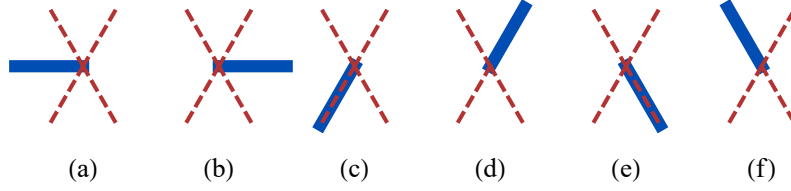


FIG. 12. Diagrams illustrating the three types of  $\langle i_1 i_2 \rangle$  bond in  $j_{pa}^x$  corresponding to  $\{(a), (b)\}$ ,  $\{(c), (d)\}$  and  $\{(e), (f)\}$ . They are denoted by the solid blue lines. For a given solid bond, there are several  $\langle i_3 i_4 \rangle$  bonds in  $j_{ap}^y$ , which combine with  $\langle i_1 i_2 \rangle$  to give a nonzero contribution towards  $\mathcal{N}$ . They are denoted by red dashed lines.

We illustrate the computation of  $Q_{i_1 i_2 i_3 i_4}^{i_5 i_6}$  using the following concrete example. Suppose that  $\langle i_1 i_2 \rangle = \boldsymbol{\delta}_1$ , i.e.  $i_2 = i_1 + \boldsymbol{\delta}_1$ . There are only eight  $\langle i_3 i_4 \rangle$  bonds contributing to  $\mathcal{S}$  as sketched in Fig.12(a-b).  $\langle i_1 i_2 \rangle$  is denoted by the blue bonds, while  $\langle i_3 i_4 \rangle$  is denoted by the red dashed bonds. The common feature is that either  $i_1$  or  $i_2$  is equal to  $i_3$  or  $i_4$ . For  $i_3 = i_2$  and  $i_4 = i_3 + \boldsymbol{\delta}_3$ ,  $i_5$  and  $i_6$  correspond to the dangling end points, namely  $(i_5, i_6) = (i_1, i_4)$  since  $i_2$  is glued to  $i_3$ .

The hopping matrix element,  $\langle P\mathbf{k}n | p_{i_5}^\dagger p_{i_6} | P\mathbf{k}n \rangle$ , is hard to compute analytically since it requires solving the Hofstadter model for the parallel sector. Therefore, for the sake of deriving the scaling relation, we assume that it is given by a value corresponding to a uniform ferromagnetic spin texture with  $\mathbf{S}_i = \hat{z}$ , where  $|P\mathbf{k}n\rangle \rightarrow |\mathbf{p}\uparrow\rangle$  and  $p_i^\dagger \rightarrow c_{i\uparrow}^\dagger$ .  $\mathbf{p}$  can be determined by  $\mathbf{k}$  when viewing that the SkX BZ is obtained by folding the BZ of the Bravais triangular lattice to which  $\mathbf{p}$  belong.

$$\langle P\mathbf{k}n | p_{i_5}^\dagger p_{i_6} | P\mathbf{k}n \rangle \rightarrow \langle \mathbf{p}\uparrow | c_{i_5\uparrow}^\dagger c_{i_6\uparrow} | \mathbf{p}\uparrow \rangle = \frac{e^{i\mathbf{p}\cdot\boldsymbol{\delta}_2}}{\mathcal{A}}. \quad (\text{A11})$$

This approximation works well when the SkX spin texture varies slowly in space, namely large  $L$ , such that the neighbouring spins are almost parallel. Since the result is site-independent, the sum over  $\langle i_1 i_2 \rangle$  contains only  $T_{pa, i_1 i_2}$  and  $T_{ap, i_3 i_4}$ , namely

$$\sum_{i_1 \in u.c.} T_{pa, i_1 (i_1 + \boldsymbol{\delta}_1)} T_{ap, (i_1 + \boldsymbol{\delta}_1) (i_1 + \boldsymbol{\delta}_1 + \boldsymbol{\delta}_3)} \boldsymbol{\delta}_{1,x} \boldsymbol{\delta}_{3,y}. \quad (\text{A12})$$

The following observation is useful for computing the sum. The hopping integral

$$\begin{aligned} T_{pa, i_1 i_2} &= -t \left( e^{-i\phi_{i_2}} \cos \frac{\theta_{i_1}}{2} \sin \frac{\theta_{i_2}}{2} - e^{-i\phi_{i_1}} \cos \frac{\theta_{i_2}}{2} \sin \frac{\theta_{i_1}}{2} \right), \\ &= -t [m_{i_2}^z (m_{i_2}^x - im_{i_2}^y) - m_{i_1}^z (m_{i_1}^x - im_{i_1}^y)], \end{aligned} \quad (\text{A13})$$

where we have re-expressed it in terms of a slowly varying auxiliary ‘‘vector field’’  $\mathbf{m}_{i_1}$  defined on each site as

$$\mathbf{m}_{i_1} = \left( \sin \frac{\theta_{i_1}}{2} \cos \phi_{i_1}, \sin \frac{\theta_{i_1}}{2} \sin \phi_{i_1}, \cos \frac{\theta_{i_1}}{2} \right). \quad (\text{A14})$$

We have checked that, at large  $L$ , the SkX spin texture defined in Section II indeed leads to a smooth  $\{\mathbf{m}_{i_1}\}$  which can be approximated by a continuum vector field  $\mathbf{m}(\mathbf{r})$ , where

$$\mathbf{m}_{i_1} \approx \mathbf{m} - \boldsymbol{\delta}_1 \cdot \nabla \mathbf{m}, \quad (\text{A15})$$

$$\mathbf{m}_{i_2} \approx \mathbf{m}, \quad (\text{A16})$$

$$\mathbf{m}_{i_3} \approx \mathbf{m}, \quad (\text{A17})$$

$$\mathbf{m}_{i_4} \approx \mathbf{m} + \boldsymbol{\delta}_3 \cdot \nabla \mathbf{m}. \quad (\text{A18})$$

The Taylor expansion is expanded around the common site  $i_2 = i_3$ . After converted into an integral, the summation, therefore, becomes

$$\frac{2t^2}{\sqrt{3}} \int_{u.c.} d\mathbf{r} \frac{\sqrt{3}}{2} (-\boldsymbol{\delta}_1 \cdot \nabla m^z (m^x - im^y) + m^z \boldsymbol{\delta}_1 \cdot \nabla (m^x - im^y)) (\boldsymbol{\delta}_3 \cdot \nabla m^z (m^x + im^y) - m^z \boldsymbol{\delta}_3 \cdot \nabla (m^x + im^y)).$$

This integral can be computed using the circular ansatz defined in the main text. After including the contributions from other bond combinations listed in Fig.12, we obtain the final result for  $\mathcal{N}$  which is purely imaginary:

$$\mathcal{N} = i\pi\sqrt{3}N_{sk} \left( \frac{te}{\hbar} \right)^2 \int_{E_{\mathbf{p}\uparrow}^{FM} < \mu_{FM}} \frac{d\mathbf{p}}{(2\pi)^2} \left[ \cos p_x + \cos \sqrt{3}p_y + 2 \cos \frac{p_y \sqrt{3}}{2} \left( \cos \frac{p_x}{2} + \cos \frac{3p_x}{2} \right) \right], \quad (\text{A19})$$

where we have converted  $\sum_{\mathbf{p}} \rightarrow \mathcal{A} \int \frac{d\mathbf{p}}{(2\pi)^2}$ . The summation over the occupied bands is estimated by the ferromagnetic value corresponding to the dispersion  $E_{\mathbf{p}\uparrow}^{FM}$  of the parallel sector and the chemical potential  $\mu_{FM}$  determined by the electron density.

Therefore, the area  $\mathcal{S}$  is indeed proportional to the skyrmion density  $N_{sk}/\mathcal{A}$ .

$$\mathcal{S} \approx \frac{e^2}{\hbar^2} \frac{\pi t^2}{J_H} \frac{N_{sk}}{\mathcal{A}} \mathcal{F}, \quad (\text{A20})$$

$$\mathcal{F} = \pi\sqrt{3} \int_{E_{\mathbf{p}\uparrow}^{FM} < \mu_{FM}} \frac{d\mathbf{p}}{(2\pi)^2} \left[ \cos p_x + \cos \sqrt{3}p_y + 2 \cos \frac{p_y\sqrt{3}}{2} \left( \cos \frac{p_x}{2} + \cos \frac{3p_x}{2} \right) \right]. \quad (\text{A21})$$


---